Functionalized biobased composite for metal decontamination – Insight on uranium and application to water samples collected from wells in mining areas (Sinai, Egypt)

Mohammed Hamza, Amr Fouda, Yuezhou Wei, Ibrahim El Aassy, Saad Alotaibi, Guibal Eric, Noha Mashaal

Functionalized biobased composite for metal decontamination – Insight on uranium and application to water samples collected from wells in mining areas (Sinai, Egypt)

Mohammed F. Hamza [a,b], Amr Fouda [c], Yuezhou Wei [a,d,*], Ibrahim E. El Aassy [b], Saad H. Alotaibi [e], Eric Guibal [f,*], Noha M. Mashaal [g]

[a] School of Nuclear Science and Technology, University of South China, Heng Yang 421001, China
[b] Nuclear Materials Authority, POB 530, El-Maadi, Cairo, Egypt
[c] Botany and Microbiology Department, Faculty of Science, Al-Azhar University, Nasr City, Cairo 11884, Egypt
[d] School of Nuclear Science and Engineering, Shanghai Jiao Tong University, Shanghai, China
[e] Department of Chemistry, Turabah University College, Taif University, P. O. Box 11099, Taif 21944, Saudi Arabia
[f] Polymers Composites and Hybrids (PCH), IMT Mines Ales, Alès, France
[g] Department of Geology, Faculty of Science, Menoufia University, Shebin El-Kom, Egypt

A B S T R A C T

A new sorbent was designed by functionalization of a bio-based composite made of chitosan and Arabic gum. The grafting of two sulfonate-bearing moieties allows reaching, at the optimum pH (i.e., pH_0 4), a sorption capacity as high as 1.48 mmol U g^{-1} (with strong affinity; b_L being close to 356 L $mmol^{-1}$). The Sips equation fits better sorption isotherms than the Langmuir equation. The maximum sorption capacity increases with temperature (while the affinity coefficient does not follow a continuous trend). The sorption kinetics are very fast; 20 min of contact are sufficient for reaching the equilibrium and the kinetic profiles are successfully fitted by the pseudo- first order rate equation. HCl solutions (0.2 M) are highly efficient for completely desorbing bound uranyl ions; the loss in sorption efficiency does not exceed 3% after 5 re-use cycles. At pH above 4, the sorbent shows high selectivity against Ca(II), Mg(II), Al(III) and Zn(II) (against Fe(III) and Cu(II), to a lesser extent). The sorbent is successfully tested for the decontamination of water samples collected from five wells located in Sinai (Egypt): uranium removal approaches 100%; metal ions like Cu(II), Fe(III), Zn(II) and Pb(II) are also remarkably recovered from samples at pH_0 5.5. Complementary tests (using agar well diffusion method) show that the sorbent brings an additional antimicrobial activity against *S. aureus*, *B. subtilis*, *E. coli*, *P. aeruginosa,* and *C. albicans*, with MIC values ranging between 50 and 25 μg mL^{-1}. The sorbent is characterized by negligible toxicity, using the MTT assay method against two normal cell lines (i.e., Vero and HFB4), and a cancerous cell line (i.e., Caco-2).

Keywords:
Functionalization of chitosan/Arabic gum composite
Uranium sorption isotherms and uptake kinetics
Application as water treatment for decontamination of groundwater collected from wells
Antimicrobial effect and cytotoxicity

1. Introduction

The growing demand for water becomes a worldwide challenge. This is especially critical for arid countries for fulfilling domestic, agriculture, and industrial uses. Water supply became also a geopolitical challenge, very sensitive for populations and regional governments. As an example, the Grand Ethiopian Renaissance Dam (GERD), which is supposed to control the Nile River in its upper part (Blue Nile), is important for Ethiopian people, but will also directly influence the human and agriculture activities in Egypt [1]. Indeed, about 68% of water uses are coming from surface water collected from the River whereas groundwater contributes by around 11% of the annual water budget from both shallow and non-renewable fossil aquifers [2]. The paucity of water and the deficit in annual water balance make the debate between Egypt, Sudan and Ethiopia a risky concern [3].

Several strategies may be developed for improving the availability of water resources; first of all improving the recycling of wastewater by innovative water treatments, but also increasing the use of groundwater resources. The quality of groundwater supplies and their conformity to drinking water regulations strongly depend on the environment of

* Corresponding authors.
E-mail addresses: yzwei@usc.edu.cn (Y. Wei), eric.guibal@mines-ales.fr (E. Guibal).

drillings and wells. Indeed, industrial (including mining) [4,5], and agriculture activities may cause serious impacts to the composition of pumped water: the release of toxic compounds (dyes, pesticides, metal ions) and their infiltration may make groundwater unfit for consumption. The presence of metals can be also of geological origin [6]: the rains and floods may cause oxidation and degradation of mineralization that dissolve metal ions, which, in turn, can circulate into geological layers and contaminate groundwater flow, and involve risks for health, animals and ecosystem [7].

Whatever the final objective, meaning treatment of contaminated wastewater or decontamination of groundwater, the development of technologies for valorizing water flows by metal removal (among other pollutants) is of critical importance. Membrane technologies (inverse osmosis, distillation, or electrodialysis) are very useful for desalination purpose [8–10]; however, they require high investments and very expensive operating costs. Sorption processes are frequently used because they can be modulated to build less expensive and smaller size units, for beneficiating small communities. Usually, a preliminary treatment (coagulation-flocculation, and filtration) is operated before using sorption beds. Activated carbon is frequently employed for removing more specifically organic contaminants [1,11–13]. Other sorbents such as metal oxides have also been used typically for the removal of arsenic and other metal contaminants [14,15]. Mineral sorbents such as apatite [16], functionalized silica [17,18], metal oxides [19] have been reported for uranium recovery from dilute solutions. Recently, nanocomposites have also retained a great attention for uranium sorption [20,21]. There is still a need for developing efficient sorbents that could be used for both metal recovery and valorization, and for decontamination of groundwater for improving water supply in irrigation, and human or livestock drinking water.

Biosorbents and biopolymers have been frequently used as efficient sorbents for metal recovery [22–25]; making profit of the presence of reactive groups such as amine (in chitosan, for example, [26]) or carboxylic groups (in alginate, for example, [27,28]). These materials have also been used as encapsulating agents (by hydrogel formation [29–31]) and/or as support for functionalization [32–34]. Indeed, the presences of hydroxyl and amine groups bring high reactivity to these materials for chemical grafting. Functionalized Arabic gum (frequently associated to other biopolymer) has also been investigated for metal sorption [25,35–40]. Arabic gum was also used as support for designing active materials with antimicrobial properties by deposition of metal oxide nanoparticles [41].

In the present work, chitosan (partially deacetylated derivative of chitin) is associated with Arabic gum (through a reaction mediated by epichlorohydrin) for preparing a support that is functionalized with two reagents bearing sulfonic moieties: 2-acrylamido-2-methyl propane sulfonic acid (AMPS) and 2-[(*p*-aminophenyl)sulfonyl]ethyl hydrogen sulfate (ASES). In addition to the specific ion-exchange properties of sulfonic groups (strong cationic exchanger), their presence increases the hydrophilic behavior of the sorbent [42]. Alexandratos and co-workers reported the criteria that can control the reactivity of sorbents [43–45]. More specifically, they pointed out the importance of the multifunctionality, the inter- and intra-ligand interactions, and the hydrophilic behavior for the design of efficient and selective sorbent.

Herein, uranium retained more specifically the attention because of the potential interest for recovering uranium from ore leachates in the processing of Sinai ores, but also because of the presence of U (and other base metals) in the groundwater of some mining areas.

The study focuses on U(VI) sorption from synthetic solutions using the functionalized biobased sorbent. First, the sorbent is characterized by SEM observation, BET, TGA, titration and elemental analysis, for proving the successful functionalization of the support, and identifying its interaction with uranyl ions. In a second step, the effect of pH on U (VI) sorption is investigated, together with the uptake kinetics (at two levels of sorbent saturation) and sorption isotherms (at different temperatures). These investigations are completed by the evaluation of sorbent selectivity for U(VI) against alkali-earth and base metals, and by the investigation of metal desorption (and sorbent recycling). The last part of the work deals with the decontamination of groundwater samples collected from five wells in Sinai area (Egypt).

The antimicrobial activity of the sorbent is also investigated to assess the possibility to apply these materials also for improving biological quality of wastewater or groundwater. Two strains of Gram-positive bacteria (*Staphylococcus aureus* and *Bacillus subtilis*), two strains of Gram-negative bacteria (*Escherichia coli* and *Pseudomonas aeruginosa*), and a unicellular fungi (*Candida albicans*) are tested using agar well diffusion method [46]. In addition, the in-vitro cytotoxicity of the sorbent was evaluated using two normal cell lines (kidney of African green monkey (Vero cells) and normal human fibroblast (HFB4 cells) as well as human colorectal adenocarcinoma (Caco-2) as cancerous cell lines [47]. This is useful for verifying the harmlessness of the sorbent in case of dispersion into receiving water phase or using the sorbent in biomedical applications.

2. Materials and methods

2.1. Materials

Crude Arabic gum (food grade) was purchased from Spices and Herbs shop (Shebin El Kom, Egypt). Chitosan (Chit, degree of acetylation, DA: ≈25%), 2-[(*p*-aminophenyl)sulfonyl]ethyl hydrogen sulfate (ASES), 2-acrylamido-2-methyl propane sulfonic acid (AMPS), potassium persulfate, and N,N'-methylenebisacrylamide (MBA) were supplied by Sigma Aldrich (Darmstadt, Germany). Epichlorohydrin (EPI) was purchased from Shanghai Makclin Biochemical Co., Ltd. (Shanghai, China). Uranyl nitrate hexahydrate ($UO_2(NO_3)_2{\cdot}6H_2O$) was obtained from Spi-Supplies (West Chester, PA, USA). Acetone and dimethylformamide (DMF) were purchased from Chron Chemicals (Qionglai, China). Other reagents were Prolabo products, which were used as received.

2.2. Synthesis of sorbent

Chitosan (2 g) and potassium persulfate (0.2 g) were successively dissolved in acetic acid solution (5% w/w, 70 mL). The solution was added drop wise into a three necked flask that contained a mixture of Arabic gum (4 g) in 50 mL DMF solution. The flask (equipped with a condenser) was heated at 50 °C for 1 h, under vigorous stirring. After cooling, a mixture containing EPI (0.05 g), AMPS (2 g), MBA (0.1 g) and ASES (1 g), which were dissolved into DMF (20 mL), were added drop wise into the reactor. The mixture was stirred and heated at 75 °C under reflux for 9 h. The hydrogel was precipitated into NaOH solution (0.6%, w/w, 1 L) under stirring overnight. The precipitated hydrogel was filtered off and washed successively with water and acetone. The sorbent was air-dried for 10 h at 60 °C.

2.3. Characterization of sorbent

The morphological structure and chemical composition were characterized using a scanning electron microscope (SEM), coupled with an energy dispersive X-ray analyzer (XL30-ESEM, Philips, FEI, Thermo Fisher Scientific, Hillsboro, OR, USA). The chemical structure of the sorbent (and the U-sorbent interactions) were analyzed using FTIR spectroscopy (IR-Tracer-100 spectrophotometer, Shimadzu, Tokyo, Japan) with the KBr disc method. The thermal degradation of the sorbent was characterized using a thermogravimetric analyzer (TGA 8000, Perkin Elmer France, Villebon-sur-Yvette, France) under N_2 atmosphere (and a temperature ramp of 10 °C/min). The textural analysis of hydrogel was carried out using high speed-surface area analyzer Nova-e Series, Model 25 (Quantachrome Corporation, Anton Paar, Boynton Beach, FL, USA). The elemental analysis (i.e., C, N, O, H, P, S and Cl) of the sorbent hydrogel was quantitatively determined using elemental analyzer Vario EL cube (Elemental Analysen systeme, GmbH-

Langenselbold, Germany).

2.4. Sorption studies on synthetic solutions

Sorption (and desorption) studies were performed in batch system (agitation speed: 210 rpm) at room temperature (i.e., 22 ± 1 °C, unless otherwise stated, for example for the study of thermodynamics: 22–52 °C). A fixed volume of solution (V, L) containing a given metal concentration, C_0 (mg U L^{-1} or mmol U L^{-1}) at pH_0 4 (unless otherwise stated; for example, for the study of pH effect: pH_0 varying between 1 and 5). A fixed amount of sorbent (m, g) was added into the solution (standard sorbent dose, SD = m/V: 0.4 g L^{-1}, unless otherwise stated) under agitation. After 48 h of contact, the sample was filtrated (on 1.2 μm pore size membrane) and the residual metal concentration (C_{eq}, mmol U L^{-1}) was analyzed by ICP-OES 5100 (inductively coupled plasma optical emission spectrometer, Agilent Santa Clara CA/USA), and the sorption capacity (q_{eq}, mmol U g^{-1}) was calculated by the mass balance equation, $q_{eq} = (C_0\text{-}C_{eq}) \times V/m$. For uptake kinetics, samples were collected at fixed times for evaluating the concentration decay (using C_0: 0.44 and 2.1 mmol U L^{-1} solutions). For sorption isotherms, the initial concentration was varied in the range: 0.042–2.17 mmol U L^{-1}. The experiments were duplicated. For the study of multi-component solutions, the same procedure was used with solutions containing equimolar concentrations (i.e., 1 mol L^{-1}, except for Cu(II): 2 mmol Cu L^{-1}) of Ca(II), Mg(II), Fe(III), Al(III), Zn(II), Cu(II) and U(VI).

Desorption kinetics were also operated in batch system with the same procedure; the elution was carried out using 0.2 M HCl solutions and a sorbent dose of 1.6 g L^{-1}; the U-loaded sorbents, which were collected from uptake kinetics, were transferred to desorption test after water rinsing. For the recycling of the sorbent, the same procedure was applied (with a water rinsing step between each sorption and desorption steps): SD was 0.4 g L^{-1} for sorption and 2 g L^{-1} for desorption.

The modeling of uptake kinetics and sorption isotherms used conventional equations (Table S1) such as:

(a) pseudo-first and pseudo-second order rate equations (PFORE and PSORE), and the Crank equation (as a simplified version of the resistance to intraparticle diffusion equation, RIDE) (Table S1a).
(b) Langmuir, Freundlich, Sips and Temkin equations (Table S1b).

Relevant equations are summarized in Table S1 (see Supplementary Information). The quality of mathematical fits was evaluated using the determination coefficient (i.e., R^2), and the Akaike Information Criterion (AIC) [48]. Parameters for the models have been obtained using non-linear regression analysis with the facilities of Mathematica® software.

2.5. Application to the decontamination of water samples from Sinai wells

Water samples were collected from wells located in Sinai (See Annex A in Supplementary Information for information on the localization, geological environment, and hydrogeological context). Experiments were carried out in batch at two pH_0 values: 2 and 5.5. The sorbent dose was set to 0.2 g L^{-1}; the agitation time was fixed to 5 h and the agitation speed was maintained at 210 rpm. The temperature was set at 22 ± 1 °C.

2.6. Antimicrobial activity and cytotoxicity

2.6.1. Antimicrobial tests

The activity of synthesized hydrogel to inhibit the growth of pathogenic microbes was investigated using agar well diffusion method [46]. This antimicrobial activity was tested on Gram-positive bacteria (*Staphylococcus aureus* ATCC6538 and *Bacillus subtilis* ATCC6633), Gram-negative bacteria (*Escherichia coli* ATCC8739 and *Pseudomonas aeruginosa* ATCC9022), and unicellular fungi (*Candida albicans* ATCC10231). Briefly, 50 μL of overnight bacterial culture (adjusted at O. D. = 1.0) was seeded onto 100 mL Muller Hinton agar media (ready-prepared-Oxoid), shaking, and poured onto sterilized Petri dishes under aseptic condition. After solidification, wells (0.7 mm in diameter) were prepared and filled with 100 μL of prepared stock solution (300 μg/1.0 mL DMSO). Different synthesized hydrogel double-fold concentrations (200, 100, 50, 25, and 12.5 μg mL^{-1}) are prepared to assess the minimum inhibitory concentration (MIC, which is defined as the lowest concentration that inhibits microbial growth). Filled Muller Hinton agar plates were kept in the refrigerator for one hour to confirm the successful diffusion; afterward, the plates were incubated at 35 ± 2 °C for 24 h. At the end of the incubation period, the diameter (mm) of inhibition zones (ZOI) around each well [49] was recorded and compared for the different experimental conditions. The experiments were triplicated; the average values were plotted with their standard deviation intervals.

2.6.2. In-vitro cytotoxicity

Two normal cell lines designated as Vero cells (kidney of African green monkey) and HFB4 cells (normal human fibroblast) as well as cancerous cell lines represented by Caco-2 (human colorectal adenocarcinoma) were obtained from Holding Company for Biological Products & Vaccines (VACSERA, Dokki, Giza, Egypt). Selected normal and cancerous cell lines were inoculated onto 96-well microtiter plates at a concentration of 1×10^5 cell/well and treated by double-fold synthesized hydrogel concentrations (1000, 500, 250, 125, and 62.5 μg mL^{-1}). The treated microtiter plates were incubated at 37 °C, for 48 h. Afterward, the morphological changes in the shape of the cells were observed using an inverted microscope (Nikon, ECLIPSE Ts2, Shinjuku, Tokyo, Japan).

The in-vitro cytotoxic efficacy of synthesized hydrogel was assessed by the so-called MTT method for viability assay (MTT: [3-(4,5-dimethylthiazol-2-yl)-2,5-diphenyl tetrazolium bromide]). Incubated plates treated with the double-fold hydrogel (as for the observation tests, see above). Briefly, the selected normal and cancerous cell lines were grown separately in a 96-well microtiter plate at a concentration of 1×10^5 cell/well. The inoculated plates were treated by the previous double-fold hydrogel concentration and incubated at 37 °C for 48 h. At the end of the incubation period, MTT reagent (5 mg mL^{-1} in phosphate-buffered saline) was added; the plates were incubated under 5 % CO_2 atmosphere for 1–5 h. Afterward, the purple formazan crystal (MTT metabolic end product) was formed before being dissolved by the addition of 10% DMSO. The plates were subjected to agitation for 30 min in dark conditions. The intensity of formed color was measured at 560 nm using an ELISA (enzyme-linked immunosorbent assay) plate reader [47]. The cell viability percentages were measured according to the following equation:

$$Cell\ viability\ (\%) = \frac{Absorbance\ of\ treated\ sample}{Absorbance\ of\ control} \times 100 \quad (3)$$

All biological results presented in this study are the means of three independent replicates. The data were subjected to analysis of variance (ANOVA) by statistical package SPSS v17. The mean difference comparison between the treatments was analyzed by the Tukey HSD (Honestly Significant Difference) test at a significance level of $p \leq 0.05$.

The IC50 values were calculated using the curve-fitting (cubic spline) with Prism software (GraphPad Software, San Diego (CA), USA) by an algorithm adapted from Chambers et al. [50].

3. Results and discussion

3.1. Characterization of sorbent

3.1.1. Textural characterization – BET and SEM

The average size of sorbent particles was close to 50 μm (±7 μm). Fig. S1 shows SEM observations of the sorbent. The surface and structure of the sorbent are irregular and folded. The air-drying contributes to the shrinking of the hydrogel (and the formation of the folds). Alternative drying techniques, such as freeze-drying or drying under supercritical

CO_2 conditions, are well known for preventing this shrinking effect and offering more porosity to dry hydrogels [51,52]. It is noteworthy that after processing the sorbent (i.e., metal sorption and elution), the material seems to be more compact and the surface smoothed compared with its initial topography.

The N_2 sorption isotherms were analyzed using the BET technique (not shown); the results confirm that the sorbent is poorly porous with a specific surface area limited to 6.3 $m^2\ g^{-1}$. The BJH method allows determining the porous volume that varies between 0.073 and 0.078 $cm^3\ g^{-1}$ (adsorption and desorption branches); while the average pore size is estimated to 294 Å (adsorption) and 159 Å (desorption).

3.1.2. TGA analysis

The thermal degradation of the sorbent (under nitrogen atmosphere), followed by the TGA (Fig. S2a) and DrTG (Fig. S2b) curves, shows four steps of weight loss:

(a) below 230 °C: sorbed water is released (weight loss, WL: ≈13%), the corresponding DrTG extremum is found close to 82.5 °C.
(b) 229–445 °C: in this temperature range, the weight loss is associated with the depolymerization of the biopolymers and their linkages through acrylamide bridges (WL: ≈39%, DrTG: 264.1 °C). The diversity of reactive groups grafted on the composite materials (including different sulfur-containing compounds) makes complex the interpretation of degradation steps.
(c) 445–633 °C: the pyrolysis leads to char formation, containing probably some stable residues (WL: ≈20%, DrTG: 464.7 °C).
(d) 633–801 °C: a weak part of the residue (about 3.4%) is degraded at higher temperature (DrTG: 668.3 °C).

The water release is slightly greater than the value reported for single Arabic gum (≈9.7%) and chitosan (≈9.6%) [53]; this means that the grafting and chemical modification slightly increases the hydrophilic behavior of the sorbent. This is probably due to the presence of numerous sulfonic groups brought by the grafting of ASES and AMPS; these sulfonic groups limits the hydrophobic effect of phenolic units (from ASES). The profile of degradation is very similar to the TGA thermogram reported by Gad [54] for chitosan-AMPS copolymer. He observed that the stability of the copolymer was increased compared with those of pure components.

The pyrolysis of the sorbent leads to a total weight loss close to 75.8%: the char represents a weight residue of 24%.

3.1.3. FTIR spectroscopy

Fig. 1 shows the FTIR spectra of sorbent before and after U(VI) sorption and after five cycles of sorption and desorption. The broad band centered around 3450 cm^{-1} is assigned to the convolution of O—H and N—H stretching vibrations, while the peaks at 2926 cm^{-1} and 2866 cm^{-1} correspond to C—H stretching vibrations (Fig. 1a). A broad band is observed at 2598 cm^{-1}, which could be attributed to S-H stretching in thiol groups. More interesting are the peaks identified in the range 2000–400 cm^{-1} (Fig. 1b). The peak at 1719 cm^{-1} confirms the presence of C═O groups (stretching vibration), while the peak at 1632 cm^{-1} is assigned to N—H bending or Amide I band. The strong peak at 1288 cm^{-1} is a tracer of S═O stretching vibration that confirms the successful grafting of AMPS and ASES moieties on the composite. A series of skeletal C—O or C—C stretching vibrations at 1175, 1069 and 1008 cm^{-1} identifies the carbohydrate ring. The strong peaks at 884 and 850 cm^{-1} correspond to C—H bending vibrations. A strong peak is also identified at 578 cm^{-1}, which could be attributed to C-Cl bond, while the peak at 453 cm^{-1} is assigned to aryl disulfides (S-S stretch) and the polysulfides (S-S stretch) from ASES and AMPS moieties.

After uranyl sorption, some typical peaks appear, including the U-O bond at 900 cm^{-1}. The O—H/N—H convoluted band is slightly shifted to 2450 cm^{-1}. The S-H stretching band is also shifted from 2598 to 2534 cm^{-1}. A considerable increase in the peaks assigned to C = O groups and

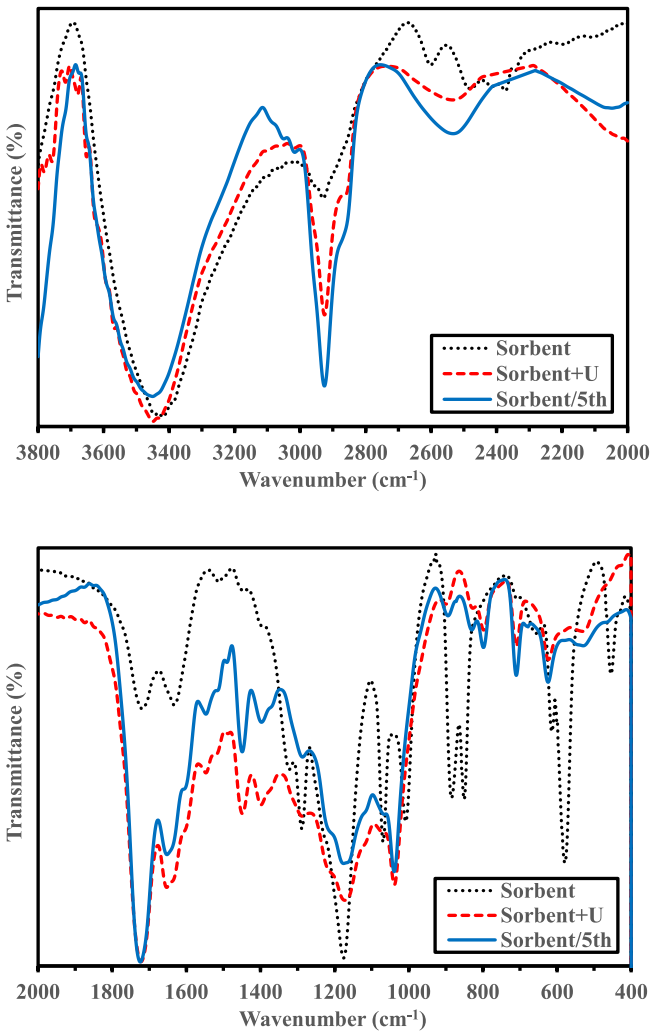

Fig. 1. FTIR spectra of sorbent, before and after U(VI) sorption (including the material after five cycles of sorption and desorption).

N–H bending/Amide I bands is also observed. Two peaks at 1448 and 1398 cm^{-1} appear much more marked than in the spectrum of the raw sorbent; they are generally assigned to C—H bending in carboxylic groups. On the opposite hand, the strong peak at 1288 cm^{-1} is significantly reduced after U(VI) sorption. The peak at 1069 cm^{-1} is drastically reduced, while the peak at 1008 cm^{-1} disappears or is shifted to 1039 cm^{-1}. The intensity of the peak at 884 cm^{-1} is strongly reduced; this signal is probably superposed with the U-O signal (at 900 cm^{-1}). The peak at 850 cm^{-1} is also considerably reduced (and shifted to 826 cm^{-1}). The strong peak at 578 cm^{-1} almost disappears (being replaced by a shoulder); as well as the signal at 453 cm^{-1}. The sorption of uranyl species affects many bands associated with amine, carboxyl and sulfonyl groups (and vicinal bonds).

The FTIR spectrum of the sorbent after five cycles of sorption and desorption almost overlaps with the spectrum of the sorbent directly after being exposed to uranyl solutions. The desorption of the metal does not restore the sorbent in its raw state. This is unexpected since the results exposed in Section 3.2.5. (relative to metal desorption and sorbent recycling) show that sorption and desorption performances are remarkably stable for five cycles. The reactive groups remain active despite the changes in the spectrum. Rather than a degradation of the sorbent, during the recycling, the changes in spectrum may be associated with the effect of ion-exchange that affects the environment of reactive groups. Fig. S3 shows the semi-quantitative EDX analysis of the sorbent before and after U(VI) sorption and after metal elution. Uranyl

sorption is clearly marked by the appearance of U signal (representing a mass fraction close to 7.4%), together with the presence of Na. The desorption is highly quantitative: U(VI) completely disappears, while Cl element appears (associated with the use of hydrochloric acid as the eluent). The relative atomic fractions are roughly maintained for C, N, and S elements, while a little decrease in observed for O element (from 47.4% to 44.9%) after metal desorption.

3.1.4. Elemental analysis

Table S3 shows the presence of S element (as a tracer of sulfonic groups) that confirms the effective grafting of the sulfonic groups brought by the grafting of AMPS and ASES compounds. The molar ratio between S and N is close to 0.128. This means that the ideal structure appearing in Scheme 1 overestimates the grafting of substituents.

3.1.5. pH_{PZC}

The pH-drift titration of the sorbent allows determining the pH_{PZC} value found close to 4.82 and 4.92 for 0.1 M and 1 M NaCl background solutions, respectively (Fig. S4). The sorbent remains protonated below pH 4.9. The maximum pH variation is reported at pH_0 4, the equilibrium pH increases by 0.5–0.7 pH unit. Above pH 4.9, the sorbent is deprotonated with anionic charges; the equilibrium pH decreases almost linearly. For the study of pH effect on uranium sorption, the pH was varied between 1 and 5 to prevent the precipitation of the metal (especially at the concentration levels used for investigating sorption isotherms). The decrease of the pH above pH 4.9 means that the sorbent is releasing protons, probably through anion exchange of Na^+.

The pH_{PZC} value of the sorbent may be influenced by the presence of numerous sulfonic groups (grafted AMPS and ASES), which are known as strong acids, and by amine groups (from chitosan, acrylamide, AMPS and ASES). The pK_a of AMPS was evaluated close to 1.67 ± 0.5, while that of ASES approaches − 3.88 ± 0.18. The pK_a of methylenebisacrylamide is close to 13.07 ± 0.18, while that of chitosan depends on the degree of deacetylation, but for most commercial samples the pK_a of amine groups is close to 6.4–6.7. Obviously, the synthesis of the sorbent strongly influences the acid-base properties of these reactive groups. However, the diversity of strongly acidic groups and basic moieties may explain that the pH_{PZC} remains acid.

3.2. Sorption properties

3.2.1. pH effect

The sorption capacity linearly increases with the pH up to pH_{eq} 4 and tends to stabilize above (Fig. 2). The speciation diagram (Fig. S5) shows that free uranyl species (UO_2^{2+}) largely predominates in the pH range 1–4. Above pH 3.5, hydrolyzed and polynuclear cationic species begin to appear; $(UO_2)_3(OH)_5^+$ predominates above pH 5. The enhancement of uranium with pH is directly controlled by the strong repulsion effect between protonated reactive groups (at low pH values) and the positively-charged metal species: the repulsion decreases as pH increases. The stabilization of sorption capacity between pH 4 and pH 5 may be explained by the dual effect of appearance of hydrolyzed and polynuclear species and the charge inversion occurring at the surface of the sorbent around pH 4.9.

The distribution coefficient ($D = q_{eq}/C_{eq}$, L g^{-1}) is plotted in log_{10} units against equilibrium pH in Fig. S6a. The slope of the curve is usually associated with the proton exchange ratio in ion-exchange reactions. Here, the slope is close to 0.57; meaning that two protons are exchanged per bound uranyl.

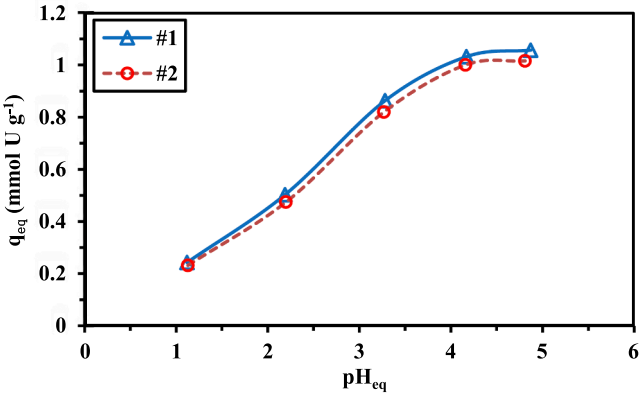

Fig. 2. Effect of pH on U(VI) sorption (C_0: 0.21 mmol U L^{-1}; Sorbent dosage, SD: 0.4 g L^{-1}; v: 210 rpm; time: 48 h; T: 22 ± 1 °C).

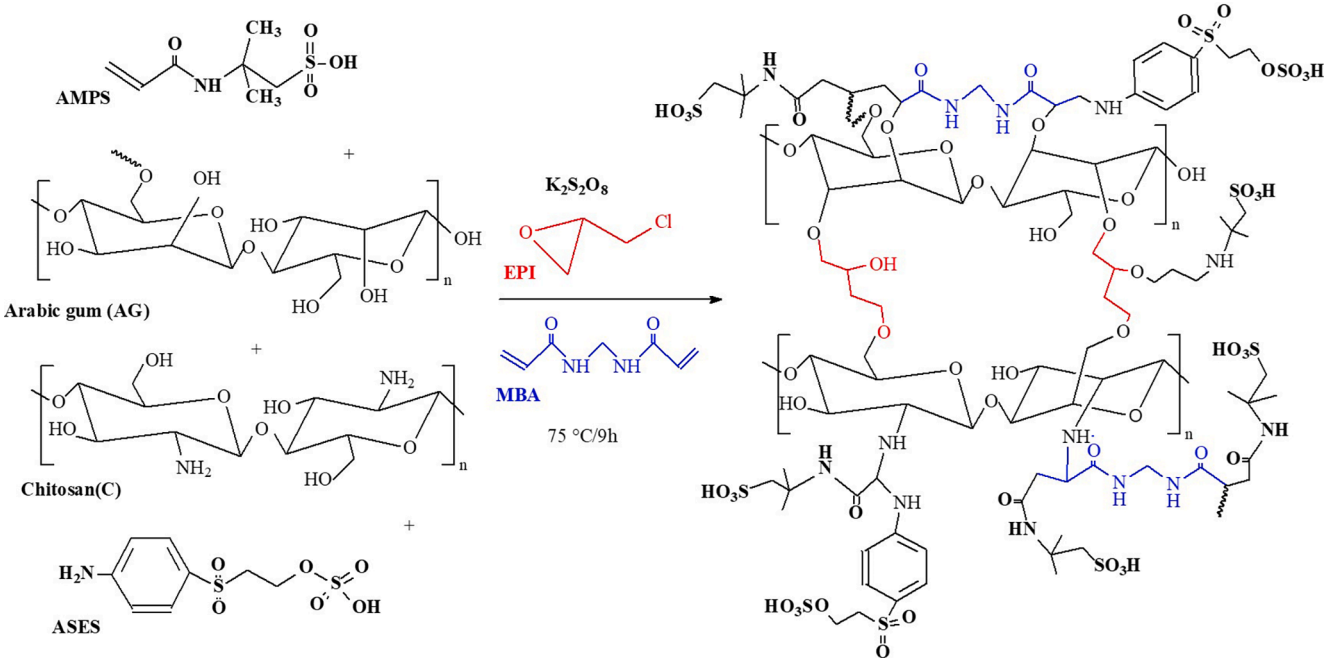

Scheme 1. Synthesis of functionalized sorbent.

It is noteworthy that the pH variation recorded during metal sorption remains very limited (Fig. S6b): slight increase between pH 1 and 4, while the equilibrium pH tends to decrease above pH 4. This is roughly consistent with the trends observed for the pH-drift titration of the sorbent. However, it is noticeable that the pH variation is less marked (lower than 0.3 pH unit) than in NaCl solutions. The sorption of uranyl tends to level off the pH variation.

For both preventing metal sorption and optimizing the sorption performance, pH_0 4 was selected for further studies on synthetic solutions. The performance of the sorbent is remarkably reproducible: the duplicate experiments are perfectly superposed.

3.2.2. *Uptake kinetics*

Different steps may affect the kinetics of sorption: the resistance to bulk, film, and intraparticle diffusion, but also the proper reaction rate. The small size of sorbent particles (around 50 μm) logically reduces the contribution of the resistance to intraparticle diffusion: the diffusion path is obviously limited. Selecting small size particles allows smoothing the limiting effect of poorly porous material. Reducing the size of sorbent particles logically increases the external surface of the sorbent (higher surface/mass ratio), which, in turn, limits the contribution of the resistance to film diffusion to the control of kinetics. Providing a sufficient agitation speed (herein 210 rpm) also avoids limiting the resistance to mass transfer through bulk diffusion effect. These preliminary remarks explain that the sorption is relatively fast (as shown in Fig. 3): a contact time of 20-30 min is sufficient for reaching the equilibrium.

The profiles have been fitted using conventional models such as the pseudo-first and pseudo-second order rate equations, and the Crank equation (Table S1a). Fig. 3 reports the fitting of experimental curves with the PFORE, while the PSORE and the RIDE models (Crank equation) are represented in Fig. S7. Table 1 summarizes the parameters of these models, together with associated statistical parameters (i.e., determination coefficient, R^2, and the Akaike Information Criterion, AIC). The discussion of preferential fit with either the PFORE or the PSORE was frequently correlated with sorption mechanisms. Hubbe et al. [55] recently demonstrated that inappropriate experimental conditions (metal concentration and sorbent dose) lead to inexact conclusions. In most cases, the strong variation of solute concentration in the solution precludes on concluding on the effective sorption mechanism. Therefore, the interpretation of model preference must be moderated and, herein, the use of these models is limited to comparing the profiles. The PFORE is definitively more appropriate for modeling experimental profiles (higher R^2 and lower AIC values, calculated q_{eq} values are closer from experimental sorption capacities). The apparent rate coefficient (i.e., k_1) is significantly increased when the concentration of the metal increases: 0.142–0.148 min^{-1} at C_0: 0.44 mmol U L^{-1}, and up to 0.226–0.217 min^{-1} at C_0: 2.11 mmol U L^{-1}. This enhancement may be explained by the favorable effect of increasing the gradient of concentration.

Table 1
Modeling of U(VI) uptake kinetics.

Model	Parameter		U concentration (mmol U L^{-1})			
			0.44		2.11	
		Series	#1	#2	#1	#2
Experimental	$q_{eq,exp.}$	mmol U g^{-1}	1.014	1.028	1.630	1.641
PFORE	$q_{eq,1}$	mmol U g^{-1}	1.038	1.052	1.629	1.628
	k_1	min^{-1}	0.148	0.142	0.226	0.217
	R^2	–	0.981	0.979	0.998	0.991
	AIC	–	−69	−68	−123	−107
PSORE	$q_{eq,2}$	mmol U g^{-1}	1.194	1.219	1.793	1.802
	k_2	L mmol^{-1} min^{-1}	0.151	0.140	0.178	0.167
	R^2	–	0.948	0.947	0.982	0.984
	AIC	–	−58	−58	−99	−100
RIDE	$D_e \times 10^9$	m^2 min^{-1}	0.456	0.414	2.36	2.20
	R^2	–	0.932	0.930	0.990	0.988
	AIC	–	−55	−54	−107	−105

The application of the Crank equation to experimental profiles shows a relatively good fit for the highest metal concentrations (AIC close to the values reported for PFORE). With C_0: 2.11 mmol U L^{-1}, the equilibrium sorption capacity tends to 1.64 mmol U g^{-1}; this is close to the saturation of the sorbent (see below, Section 3.2.3). The effective intraparticle diffusion coefficient is close to 2.3×10^{-9} m^2 min^{-1}; this is only one order of magnitude lower than the self-diffusivity of uranyl in water (i.e., 2.56×10^{-9} m^2 min^{-1}, [56]). This is another confirmation that the resistance to intraparticle diffusion is not playing a critical role in the sorption of uranyl onto the sorbent. The large size of pores (compared with the hydrated radius of uranyl: 16–29 nm *vs.* 0.24–0.28 nm) and the diffusion length may explain that uptake kinetics may be controlled by the proper reaction rate (modeled by the PFORE). Worse fits are observed at C_0: 0.44 mmol U L^{-1} (residual relative concentration being below 0.1, leading to higher discrepancy in modeling). The saturation of the sorbent is not reached and sorption is probably limited to the external layers of the sorbent; therefore, the Crank modeling is less accurate.

3.2.3. *Sorption isotherms and thermodynamics*

The sorption isotherms are reported in Fig. 4 for different temperatures (ranging between 22 °C and 52 °C). The high affinity of the sorbent for uranyl is clearly illustrated by the steep initial slope (almost vertical); this type of profile is usually associated with irreversible sorption. The sorption isotherms are also characterized by asymptotic trends that correspond to saturation plateaus (≈ monolayer saturation in the Langmuir model). The maximum sorption capacity increases with

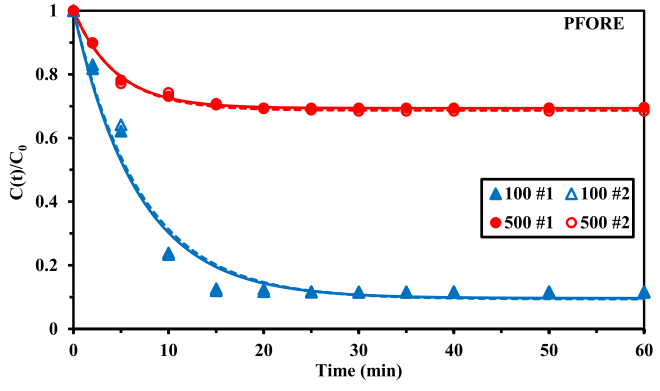

Fig. 3. U(VI) uptake kinetics – PFORE modeling (pH_0: 4; pH_{eq}: ~4.15; SD: 0.4 g L^{-1}; C_0: 100 and 500 mg U L^{-1}; 0.44 and 2.11 mmol L^{-1}; v: 210 rpm; T: 22 ± 1 °C).

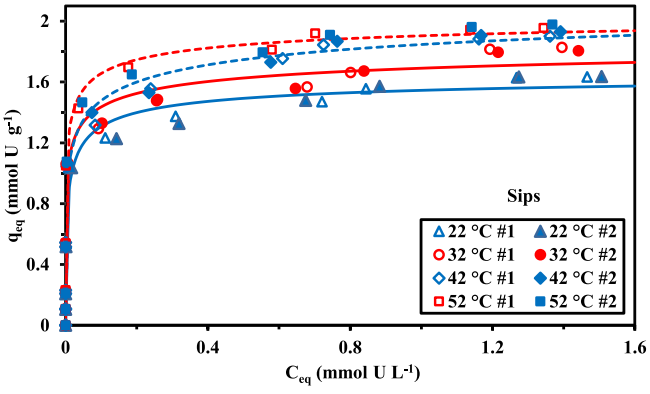

Fig. 4. U(VI) sorption isotherms at pH_0 4 – Sips modeling (pH_{eq}: ~4.13–4.35; SD: 0.4 g L^{-1}; C_0: 0.4–2.13 mmol U L^{-1}; v: 210 rpm; T: 22 ± 1 °C, time: 48 h).

temperature from 1.64 to 1.98 mmol U g^{-1}. The sorption of uranyl onto the sorbent is an endothermic mechanism. Zidan et al. [57] also found endothermic uranyl sorption onto Duolite aminophosphonic resin, contrary to Giannakoudakis et al. [58], who reported the uranium binding onto phosphonate-functionalized mesoporous to be exothermic.

The comparison of maximum sorption capacity with the elemental composition of the sorbent clearly demonstrates that the sorption occurs not only onto sulfonic groups (only 0.64 mmol S g^{-1}) but also on amine groups (about 5 mmol N g^{-1}).

The sorption isotherms have been fitted with conventional Langmuir, Freundlich, Sips and Temkin equations (Table S1b). The parameters of these models (and relevant statistical evaluators) are summarized in Table 2. The Sips modeling is appearing as solid lines in Fig. 4; the other models are represented in Fig. S8. The Langmuir model suggests that the sorbent surface is homogeneous (same sorption energy), the sorption occurs as a monolayer and sorbate molecules are bound with mutual interactions between sorbed molecules. The Freundlich equation (which is an empirical equation, contrary to Langmuir model) is associated with systems involving lateral interactions between sorbed molecules with surface heterogeneities. The Sips equation combines the Langmuir and the Freundlich equations; the introduction of a third-adjustable parameter usually improves the quality of data fit, at the expense of a loss in physicochemical significance. The Temkin equation supposes a linear variation of the adsorption heat (correlated with the rate of coverage of sorbent surface). The comparison of statistical indicators shows that the fits follow the quality ranking: Temkin ≈ Sips ≫ Freundlich ≫ Langmuir. The Langmuir equation fails to represent the irreversible shape (initial vertical slope; the zone of maximum curvature cannot be fitted), while the saturation plateau is not consistent with the exponential Freundlich model. In the Sips equation, the sorption capacity at saturation (i.e., $q_{m,S}$) overestimates the maximum sorption capacity; however, the third-adjustable parameter allow improving the quality of the fit. The variation of the parameters (b_L, b_S or b_T) with temperature does not follow a clear linear trend; probably due to the steep initial slope that introduces strong variations in the determination of affinity coefficients (Langmuir and Sips equations) and sorption constant for Temkin equation. The discussion of thermodynamics is thus limited to concluding on the endothermic behavior of uranyl sorption. The b_T values vary between 15 and 18 kJ mol^{-1}; this order of magnitude is usually associated with physical sorption mechanism.

Table S4 compares U(VI) sorption properties of alternative sorbents. The sorbent shows outstanding sorption performances compared with sorbents recently investigated: the sorption capacity is among the highest values reported in literature (1.48 mmol U g^{-1} with affinity coefficient close to 356 L $mmol^{-1}$). Amesh et al. [59] recently reported much higher sorption capacities (close to 4.48 mmol U g^{-1}) using diethylenetriamine tethered mesoporous silica, but at much higher pH value (i.e., pH 6, in acetate solution, with possible occurrence of precipitation phenomena at the highest concentrations used for establishing isotherms). Phosphonate-functionalized mesoporous silica exhibits little faster sorption [58], but with lower sorption level and affinity. He et al. [60] reported sorption capacity comparable for amidoximated marine fungus mycelium (about 1.56 mmol U g^{-1}) but with much lower affinity coefficient (≈0.38 L $mmol^{-1}$). The sorbent represents an excellent compromise taking into account the combination of criteria such as kinetic, sorption capacity and affinity coefficients.

Table 2
Modeling of U(VI) sorption isotherms.

Model	Parameter		Temperature (°C)			
			22	32	42	52
Experimental	$q_{m,exp.}$	mmol U g^{-1}	1.64	1.83	1.93	1.98
Langmuir	$q_{m,L}$	mmol U g^{-1}	1.48	1.57	1.73	1.79
	b_L	L $mmol^{-1}$	356.0	2639	402.9	1105
	R^2	–	0.953	0.933	0.940	0.954
	AIC	–	−79	−72	−66	−72
Freundlich	k_F	$mmol^{1-1/n}$ g^{-1} $L^{1/n}$	1.60	1.75	1.89	1.99
	n_F	–	5.86	6.83	6.53	6.91
	R^2	–	0.951	0.954	0.970	0.958
	AIC	–	−78	−91	−105	−88
Sips	$q_{m,S}$	mmol U g^{-1}	1.69	1.99	2.40	2.12
	b_S	L $mmol^{-1}$	10.5	5.71	3.37	8.67
	n_S	–	2.03	2.94	3.12	2.57
	R^2	–	0.978	0.970	0.983	0.988
	AIC	–	−91	−94	−115	−109
Temkin	$A_T \times 10^{-3}$	L $mmol^{-1}$	18.34	156.2	111.1	194.7
	b_T	kJ kg mol^{-2}	15.25	17.69	16.56	17.00
	R^2	–	0.984	0.954	0.986	0.989
	AIC	–	−99	−94	−125	−99

3.2.4. *Sorption selectivity*

The diversity of functional groups at the surface of the sorbent may involve affinity for different metal ions, at the expense of competition effects that reduce the binding of target metal. Therefore, investigating the sorption preferences of the sorbent using multi-component solutions is of critical importance, taking into account the pH of the solution. The sorption capacities increase with the pH (not shown). In the case of U (VI), the sorption capacities reach 1.04–1.09 mmol U g^{-1} (for C_0: 1 mmol U L^{-1}); this is about 30% less than the sorption capacity reported in sorption isotherms for mono-component solutions. The selectivity coefficient $SC_{U/metal}$ is defined as the ratio of distribution coefficients, according eq. (1):

$$SC_{U/Metal} = \frac{D_U}{D_{Metal}} = \frac{q_{eq,U} \times C_{eq,Metal}}{q_{eq,Metal} \times C_{eq,U}} \quad (1)$$

Fig. 5 compares the SC values referred to U(VI) (Fig. 5a) and Cu(II) (Fig. 5b). The selectivity of the sorbent for U(VI) increases with the pH: highest SC values are obtained at pH_{eq} 4.17 and 4.87. At pH_{eq} 4.87, the

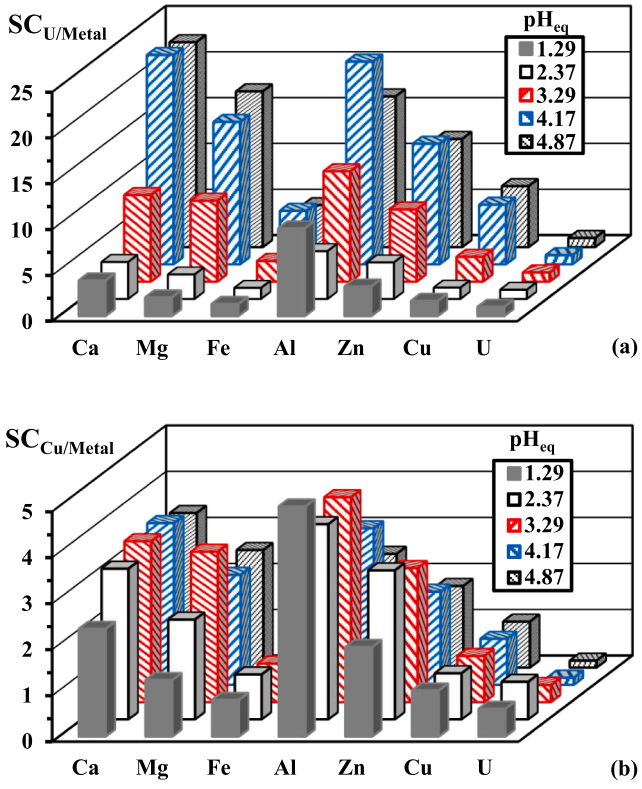

Fig. 5. Effect of pH on sorbent selectivity for U(VI) (a) and Cu(II) (b) against competitor metal ions (C_0: 1 mmol L^{-1}, except 2 mmol Cu L^{-1}; SD: 1 g L^{-1}; time: 24 h; T: 22 ± 1 °C; v: 210 rpm).

selectivity increases according:

Fe(III) [5.8] ≈ Cu(II) [6.6] < Zn(II) [13.2] < Mg(II) [17.0] << Al(III) [22.1] ≈ Ca(II) [22.8]

In the case of Cu(II), the sorption capacity increases with pH from 0.188 to 0.909 mmol Cu g^{-1}. However, Fig. 5b shows that the selectivity for copper against other metal ions is less affected by the pH than for U (VI); whereas the SC values are much lower (systematically below 6). The sorbent shows a remarkable selectivity for U(VI) against alkali-earth metals and base metals, especially at pH higher than 4.5. Table S5 reports the main physicochemical properties of selected metals. The HSAB principle (hard and soft acid and base theory, as defined by Pearson [61]) states that hard acids preferentially react with hard bases. The sorbent bears sulfonic groups (i.e., hard base) and amine groups (i.e., soft base). On the other side, all selected metal ions are hard acids, except Zn(II) and Cu(II) that are borderline. The coexistence of sulfonic and amine groups may explain the difficulty in correlating the preference scale for metals with their HSAB ranking. The same difficulty is observed when considering the other criteria (hydrated radius, softness, solution-phase electronegativity, Pauling electronegativity or hydration enthalpy) reported in Table S5.

Fig. S9 plots the distribution coefficients (in $\log_{10}$ unit) for selected metals *vs.* the equilibrium pH. Table S5 reports their slope analysis. Compared with mono-component solutions, the slope for U(VI) slightly decreases (from 0.57 to 0.44), but remains higher than for other metal ions (in the range 0.14 to 0.32). For U(VI), the slope analysis is consistent with the ion-exchange of UO_2^{2+} with two protons; this is also consistent in the case of Al(III) (slope ≈ 0.32, with Al^{+3} exchanged with 3 protons). For the other metal ions, the slopes are not coherent with possible stoichiometric ratio; another type of mechanism may be involved in metal uptake, including chelation. Table S5 also reports the distribution coefficients at pH_{eq} 1.29 and 4.87. At mild pH, the preference of the sorbent for U(VI) is confirmed by the much higher value of the distribution ratio (4 to 20 times the D values for other metals).

3.2.5. Metal desorption and sorbent recycling

Although sorption isotherms and uptake kinetics are important criteria for evaluating the potential of a sorbent, its competitiveness must also take into account other parameters such as the reversibility of the sorbent (metal desorption) and its re-usability. The investigation of the pH effect showed that U(VI) sorption is strongly controlled by the pH and the protonation of reactive groups. It is thus possible anticipating that acidic solutions can be useful for eluting U(VI) from metal-loaded sorbent. Fig. S10 reports the desorption kinetics of the sorbent (loaded with uranyl during the study of uptake kinetics) using 0.2 M HCl solutions. The figure demonstrates: (a) the good reproducibility in the profiles of desorption, (b) the efficient elution of the sorbent (complete desorption), (c) the fast desorption (within 20 min of contact, about 30 min for the sorption step), and (d) the slightly faster desorption when the sorbent is not fully saturated (sorbents collected after treatment with 0.44 mmol U L^{-1}). Table 3 compares the sorption and desorption efficiencies for five successive cycles of sorption and desorption (under the same experimental conditions). At the fifth cycle, the loss in sorption remains below 3%; on the other hand, uranyl is fully desorbed at each step. The sorbent shows a remarkable stability in terms of sorption and desorption performances. This is especially noticeable because the FTIR spectrum of the sorbent after five cycles of sorption and desorption is apparently significantly changed compared with the spectrum of pristine sorbent (see Section 3.1.3.). The changes in the spectrum may reflect protonation and/or ion-exchange effect, which is not affecting sorption efficiency.

3.3. Application to the decontamination of underground water samples

3.3.1. Metal removal by sorption

The sorbent was tested for the removal of selected metal ions from samples collected in wells from mining areas of Sinai (Egypt). More details on their localization and their geological characteristics (See Annex 1) may directly influence the composition of water samples (their composition is reported in Table S6). These samples are characterized by their strong salinity with concentrations varying between 0.94 and 2.22 g Cl^- L^{-1}, 0.01 and 0.067 g SO_4^{2-} L^{-1} (nitrate and phosphate concentrations remaining below 2 and 21 mg L^{-1}, respectively). As a corollary, alkali and alkali-earth elements are predominating: 1.13–2.23 g Na L^{-1}, 0.24–0.33 g Ca L^{-1}, and 0.11–0.22 g Mg L^{-1}. The concentrations of heavy metals are significantly lower: less than 16 mg Cu L^{-1}, 8 mg Fe L^{-1}, 25 mg Zn L^{-1}, 3.3 mg Pb L^{-1}, and 4.3 mg U L^{-1}. For some of these metal ions, the levels exceed the maximum concentrations fixed for drinking water, irrigation water or livestock drinking water (as reported in Table S7). Therefore, the sorbent was subjected to sorption process, for 5 h, at two pH values: (a) ≈2-2.5, and (b) ≈6-6.5. The sorbent dosage was set to 0.2 g L^{-1}. Consistently, with previous results, the sorption of metal ions increases with the pH. Fig. 6a shows that at pH 2, the sorption never exceeds 78%, regardless of the metal ions (including those found at very low concentration) and the wells. The protonation of the sorbent limits its capacity to bind those selected metal ions. On the other hand, at pH ≈5.5 (Fig. 6b), the sorption of alkali-earth metals is slightly increased but due to their huge excess the sorption efficiencies only vary between 5% and 18%; while for heavy metals, in most cases, the sorption efficiency exceeds 89%. It is notably that uranium is fully removed for all wells. For the other heavy metals, the decontamination levels depend on the wells: the more efficient removals are reported for wells SH1 and SH2. The most problematic issues are reported for lead recovery from samples AG1, AG2 and AG3. This is probably associated with the high concentrations of chloride ions, and higher levels of heavy metals (compared with SH1 and SH2 samples).

Fig. S11 compares the distribution coefficients for heavy metals after the treatment of the different wells. The distribution coefficient ($D = q_{eq}/C_{eq}$, L g^{-1}) is obviously controlled by the initial concentrations (the alkaline and alkali-earth metals that are present in large excess are not taken into account in this comparison). Despite the different levels of concentrations, the D values offer an opportunity to compare the affinity of the sorbent for the metals. Uranium (with D values ranging between 2714 and 6919 L g^{-1}) shows a greater affinity and enrichment on the sorbent; followed by lead (D less than 2328 L g^{-1}) and, to a lesser extent, copper (in SH1 and SH2 wells, less than 1123 L g^{-1}), and zinc in AG1 and AG2 wells (less than 1237 L g^{-1}). The major elements (Mg, Ca and

Table 3
Metal desorption and sorbent recycling: sorption (SE, %) and desorption (DE, %) efficiencies.

Cycle	Series #1				Series #2			
	SE		DE		SE		DE	
	Aver.	St.Dev.	Aver.	St.Dev.	Aver.	St.Dev.	Aver.	St.Dev.
#1	95.6	0.7	99.8	0.2	95.5	0.3	100.0	0.0
#2	95.3	0.7	99.9	0.1	94.8	0.4	99.6	0.5
#3	94.5	0.8	100.0	0.1	94.4	0.2	99.7	0.3
#4	93.9	0.6	99.7	0.4	93.5	0.7	100.5	0.7
#5	93.4	0.3	99.9	0.3	92.7	0.5	99.6	0.1
Loss $5^{th}/1^{st}$	less than 3%		Negligible		less than 3%		Negligible	

(Adsorption/pH_0: 4; C_0: 0.44 mmol U L^{-1}; SD: 0.4 g L^{-1}; time: 24 h – Desorption/0.2 M HCl solution; SD: 2 g L^{-1}; time: 2 h – Agitation: 210 rpm; T: 22 ± 1 °C).

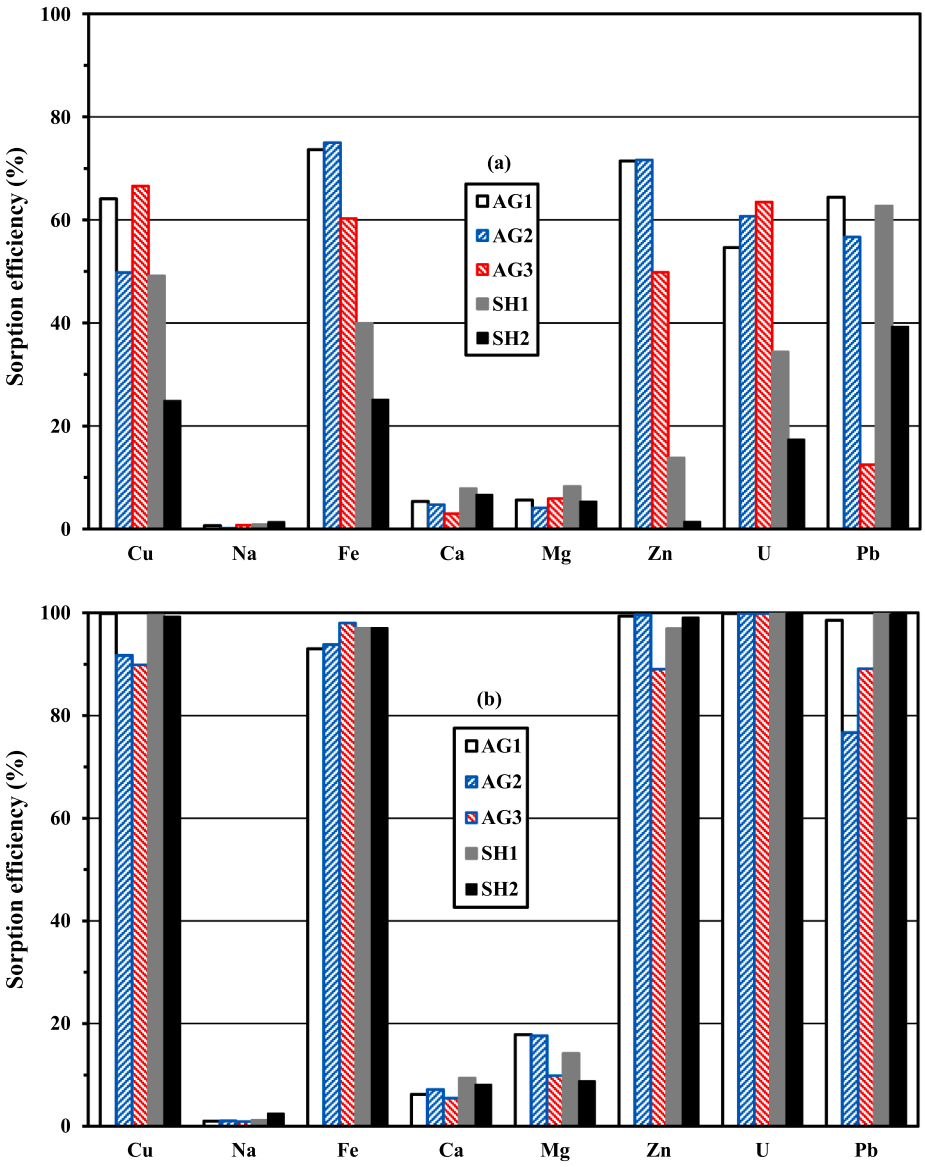

Fig. 6. Sorption efficiency for the treatment of water samples collected from Sinai wells after pH control at (a) pH_0 ≈2 and (b) pH_0 5.5 (SD: 0.2 g L^{-1}; time: 5 h; T: 22 ± 1 °C; v: 210 rpm).

Na) are not shown but their D values are systematically below 1.1 L g^{-1}. These data clearly confirm the selectivity of the sorbent for uranyl against other heavy metals, despite the high salinity of the solutions (and huge concentrations of chloride and sulfate anions).

Fig. S12 summarizes the EDX spectra of the sorbent exposed to samples collected from the different wells at pH_0 5.5. The analysis shows the wide activity of the sorbent for the different metals present in the water samples. Many heavy metals are identified, in addition to alkali and alkali-earth metals, but also Cl element -counter-anion Cl^-). Table S8 compiles the semi-quantitative EDX analysis of the sorbent after being in contact with the water samples collected in the different wells. These data confirm the wide-spectrum of the sorbent in terms of metal affinity. Highest U(VI) concentrations are reported on sorbent exposed to AG1 and AG2 water samples, consistently with the highest concentrations of uranyl in collected samples.

Table S9 summarizes the residual concentrations of heavy metals after sorption step at pH ≈5.5, and confronts these levels to the regulations for drinking water (human and livestock) and irrigation purposes. The sorption treatment is sufficient for clearing the contamination of water samples with uranium and lead. Wells SH1 and SH2 are conform for use in irrigation and livestock feeding; for human drinking water and Cu concentrations, it depends on regional regulations (US and WHO: fine; limit according EU standards). The treated water from AG1 can be also used for irrigation and livestock drinking purposes, however, the concentration for lead exceeds the international standards for drinking water and the level of iron may have an impact on water taste. For AG2 and AG3, the sorption process is not sufficient for reaching the standards in irrigation for copper, while for human drinking water, the concentration levels in lead are limit (depending on regional standards).

The sorption process is generally sufficient for achieving the standards for livestock drinking water; considering copper levels, it depends on the type of livestock: 0.5 mg L^{-1} for sheep, 1 mg L^{-1} for cattle, and 5 mg L^{-1} for swine and poultry. AG1, SH1 and SH2 wells can be used for feeding all types of livestock, while AG3 may be also used except for sheep. Treated water from AG2 well can only be used for drinking swine and poultry.

3.4. Antimicrobial and cytotoxicity issues

3.4.1. Antimicrobial activity

Before investigating antimicrobial activities, DMSO was tested as a blank; the tests showed no antimicrobial effect for the solvent. Interestingly, the synthesized hydrogel exhibits antimicrobial activity against all tested pathogenic microbes (Fig. 7, Fig. S13). This efficiency is dose-dependent. This is consistent with previous data reported by different teams [62–64]. The lowest concentration (i.e., 12.5 μg mL^{-1}) does not show detectable antimicrobial activity toward tested pathogenic microbes. When the amount is doubled (concentration: 25 μg mL^{-1}), only Gram-positive bacteria *B. subtilis* and *S. aureus,* and unicellular fungi *C. albicans* show effective sensitivity, characterized by the appearance of a clear zone, with diameters close to 10.2 ± 0.4, 10.5 ± 0.5, and 9.3 ± 0.6 mm, respectively.

When the concentration exceeds 25 μg mL^{-1}, all the microorganisms are polymer-responsive. For example, the zone of inhibition formed after treating with a concentration of 50 μg mL^{-1} was 11.6 ± 0.6, 11.7 ± 0.3, 10.3 ± 0.6, 11.3 ± 0.6, and 10.8 ± 0.3 mm for *B. subtilis, S. aureus, P. aeruginosa, E. coli,* and *C. albicans* respectively. These zones of inhibitions were increased due to treatment by 300 μg mL^{-1} to reach 17.7 ± 0.6, 18.0 ± 0.0, 15.7 ± 0.6, 17.7 ± 0.5, and 17.0 ± 0.0 mm, respectively. In Fig. 7, the statistical analysis confirms the significance of difference (with $p \leq 0.001$) (groups identified by distinct letters). The sensitivity of tested pathogenic microbes toward synthesized hydrogel can be ranked according to: *S. aureus* > *B. subtilis* > *E. coli* > *C. albicans* > *P. aeruginosa*.

The cell wall of Gram-positive bacteria is mainly composed of peptidoglycan (40 – 90 %), contrary to Gram-negative bacterial cell wall that contains approximately 10 % peptidoglycan surrounded by an outer membrane made of lipopolysaccharide, proteins, and phospholipid [65]. The inhibitory effect of the synthesized hydrogel may be attributed to their efficacy to break down the 1,4-β-glycosidic linkage between two monomers (i.e., N-acetyl glucosamine and N-acetyl muramic acid) in the peptidoglycan backbone. Due to cell wall hydrolysis, the active compound can enter the bacterial cell and interacts with cell components such as DNA, proteins, and amino acids, which, in turn, alter their activity [66]. Moreover, the accumulation of active compounds inside the bacterial cell may enhance the production of reactive oxygen species (ROS) and finally induce bacterial death [67,68]. Herein, the higher sensitivity of Gram-positive bacteria (compared with Gram-negative bacteria) can be explained by this type of mechanism.

Another inhibitory mechanism may be associated with the alteration of the selective permeability function of the bacterial cytoplasmic membrane, which may ultimately lead to the uncontrolled release of cell components [69,70]. Hence, the presence of 2-acrylamide-2-methyl propane sulfonic acid in the synthesized hydrogel can inactivate the extra-lipid layer present in the cell wall of Gram-negative bacteria [62].

The growth inhibition of *C. albicans* due to treatment by active compounds can be attributed to the change in the pathway of ergosterol biosynthesis. This effect may alter the sterol profile or disrupt the cell wall of unicellular fungi [71].

Data analysis showed that the MIC value (minimum concentration for inhibition of microbial growth) of synthesized hydrogel was 50 μg mL^{-1} for Gram-negative bacteria (*P. aeruginosa* and *E. coli),* whilst it was 25 μg mL^{-1} for Gram-positive bacteria (*B. subtilis* and *S. aureus*) and unicellular fungi (*C. albicans*) (Fig. 7). Besides the high activity of synthesized hydrogel for metal recovery from water solutions, the sorbent can be used to control or kill the pathogenic microbes that may be present (at low level) in contaminated water sample.

3.4.2. Cytotoxicity tests

The *in-vitro* cytotoxic efficacy of some hydrogels against normal and cancerous cell lines was investigated by various researchers [72,73]. In the current study, the cytotoxicity level of different concentrations (1000, 500, 250, 125, 62.5, and μg mL^{-1}) of the material were measured using MTT assay method against two types of normal cell lines (Vero and HFB4) and one cancerous cell line (Caco-2) (Fig. 8). The MTT is an accurate and sensitive colorimetric method used to investigate the cellular toxicity and proliferations of cells due to exposure to external substances [74]. Data showed that the morphological characteristics and cell viability of tested cell lines are dependent on the concentration used. The adverse effects are observed at high concentrations and decrease by reducing hydrogel concentration. These data are consistent with those reported by Shukla et al. [75] and Lashin et al. [76].

Fig. S14 depicts the morphological characteristic of Vero, HFB4, and Caco-2 cell lines. As shown at high concentration (i.e., 1000 μg mL^{-1}), the cells lost their ability to adhere and form a normal layer. In some cases, the cells tend to granulate, and become rounded, or shrink. The monolayer structure that characterizes the epithelial cells is destroyed, compared to untreated cells (control). At low concentration (i.e., 500 μg mL^{-1}), the Vero and HFB4 cells show normal shape, whereas cancerous

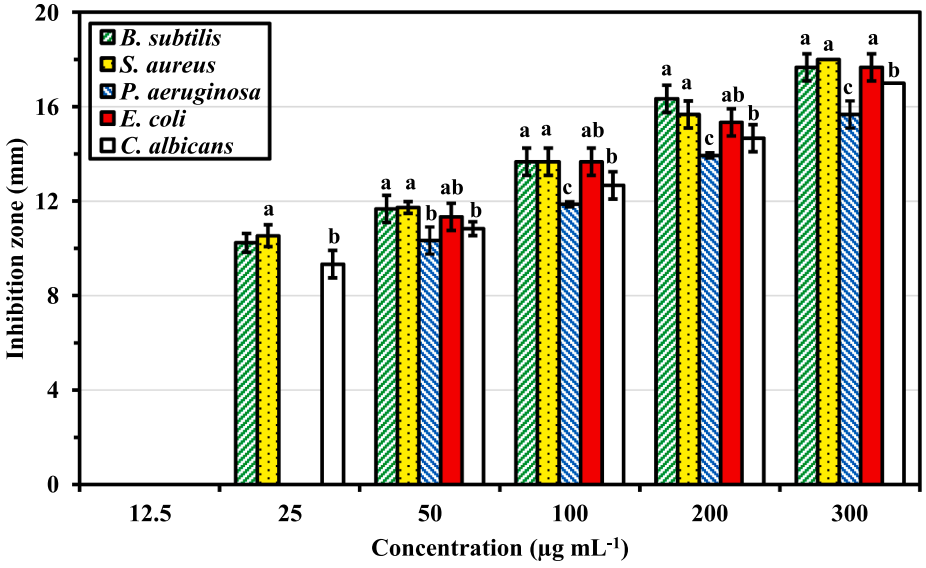

Fig. 7. Antimicrobial activity (represented by mm) of synthesized hydrogel against pathogenic microbes *Bacillus subtilis*, *Staphylococcus aureus*, *Pseudomonas aeruginosa*, *Escherichia coli*, and *Candida albicans*. Letters on bars at the same concentration represent the series with mean values that are statistically (significantly) different ($p \leq 0.05$) (n = 3).

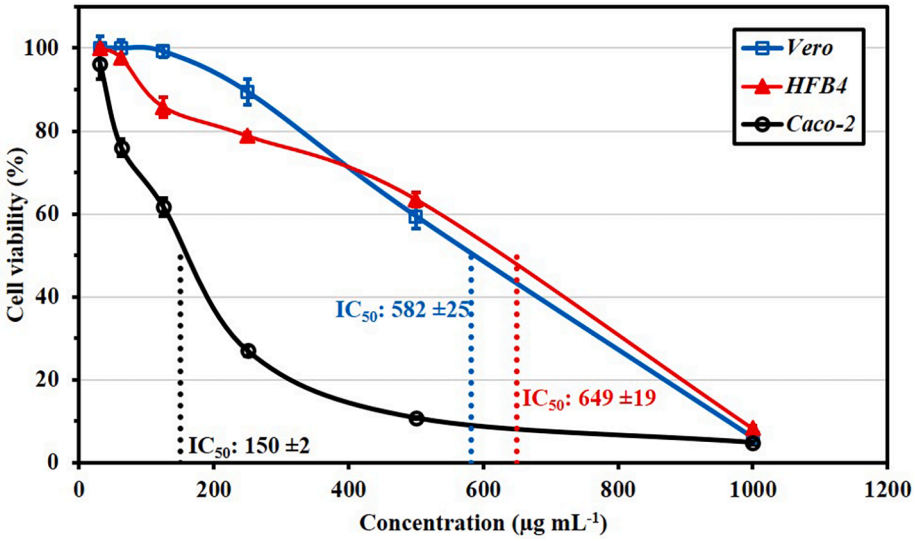

Fig. 8. MTT assay method of synthesized hydrogel against normal cell lines (Vero and HFB4) and cancerous cell lines (Caco-2).

Caco-2 cell lines are characterized by abnormal features. These abnormal features include a partial breakdown of the integral monolayer of epithelial cells. Therefore, the cells tend to be subject to shrinkage, buoyancy; they appear as rounded or spherical cells. In addition, the cell population tends to decrease. Similar trends are also observed at lower doses of material. Cell viability percentages show that the IC50 values (the concentration of material applied for achieving 50 % cell mortality) are 582.03 ± 1.7, 649.41 ± 1.5, and 149.67 ± 0.5 µg mL^{-1} for Vero, HFB4, and Caco-2 cell lines, respectively (Fig. 8). It is remarkable that the sorbent shows a significant effect on target cancerous cells at low concentration; under conditions where the normal cells are not affected. The sorbent can be used at low concentration for wastewater treatment without adverse effect on normal cells. The cellular damage caused by hydrogel can be attributed to the high production of reactive oxygen species (ROS) that causes oxidative stress and finally apoptosis [77,78]. Moreover, the interaction of cells with external substance may inhibit the synthesis of adenosine tri-phosphate (ATP) synthesis, and alter the proteins and enzymes, contributing to cell death [79].

4. Conclusions

The grafting of sulfonate reagents onto chitosan/Arabic gum composite allows binding uranyl ions through amine and sulfonic functional groups. At weakly acidic pH (i.e., pH_0 4) sorption is fast (equilibrium attained within 20 min) and highly efficient (high sorption capacity close to 1.48 mmol U g^{-1} combined with a strong b_L affinity, i.e., 356 L $mmol^{-1}$). Conventional equations fit well experimental profiles (PFORE for kinetics and Sips equation for sorption isotherm). The sorbent shows remarkable stability in terms of recycling; due to the high deficiency of 0.2 M HCl solutions for desorbing U(VI) from loaded sorbent. The sorbent has a wide spectrum of reactivity against heavy metal ions with a marked preference for U(VI) (as shown by selectivity tests).

The decontamination of water from wells in Sinai area (which are located in highly mineralized areas, with non-negligible impacts on the quality of groundwater) is of critical importance in this area. The sorbent shows high efficiency for removing uranyl and selected heavy metals. The levels of decontamination show that the sorbent can be used as a primary treatment for making well water usable for irrigation and livestock purposes. Complementary treatments would be necessary for making treated water conform to regulations for human drinking water.

It is noteworthy that the sorbent shows a significant antimicrobial activity against Gram-positive and Gram-negative bacteria, and *C. albicans*, with MIC values close to 25–50 µg mL^{-1}. This offers the sorbent a double effect as antimicrobial and decontaminating agent. In addition, preliminary tests demonstrate that the sorbent has negligible cytotoxicity.

These results demonstrate the interest of this multifunctional material for securing the water resource in areas where the geological characteristics and mining activities may cause hazardous impacts on groundwater.

Declaration of Competing Interest

The authors declare that they have no known competing financial interests or personal relationships that could have appeared to influence the work reported in this paper.

Acknowledgements

Saad H. Alotaibi acknowledges Taif University for Researchers Supporting Project (TURSP- 2020/83), Taif University, Saudi Arabia. Eric Guibal, Mohammed F Hamza and Amr Fouda acknowledge the support of IMHOTEP Program (MetalValor project, N°39525QA) from French Government (Institut Français d'Egypte) and Egyptian Academy of Science & Technology.

Appendix A. Supplementary data

Supplementary data to this article can be found online at https://doi.org/10.1016/j.cej.2021.133967.

References

[1] E.O. Orakwue, V. Asokbunyarat, E.R. Rene, P.N.L. Lens, A. Annachhatre, Adsorption of iron(II) from acid mine drainage contaminated groundwater using coal fly ash, coal bottom ash, and bentonite clay, Water Air Soil Pollut. 227 (2016) 74–85.
[2] M.E.D.M. Omar, A.M.A. Moussa, Water management in Egypt for facing the future challenges, J. Adv. Res. 7 (2016) 403–412.
[3] J.M. Mbaku, The controversy over the Grand Ethiopian Renaissance Dam, https://www.brookings.edu/blog/africa-in-focus/2020/08/05/the-controversy-over-the-grand-ethiopian-renaissance-dam/, Accessed: 08/10/2021.
[4] O.V. Omonona, A.C. Ekwe, G.-B. Azuoko, S.N. Ukpai, Assessing the groundwater quality of a small-scale mining drainage basin using modified water quality indices, Arabian J. Geosci. 14 (2021) 1566.
[5] K. Ren, J. Zeng, J. Liang, D. Yuan, Y. Jiao, C. Peng, X. Pan, Impacts of acid mine drainage on karst aquifers: Evidence from hydrogeochemistry, stable sulfur and oxygen isotopes, Sci. Total Environ. 761 (2021), 143223.

[6] M. Sakizadeh, E. Ahmadpour, Geological impacts on groundwater pollution: a case study in Khuzestan Province, Earth Environ. Sci. 75 (2015) 88.
[7] N. Devaraj, B. Panda, S. Chidambaram, M.V. Prasanna, D.K. Singh, A. L. Ramanathan, S.K. Sahoo, Spatio-temporal variations of uranium in groundwater: Implication to the environment and human health, Sci. Total Environ. 775 (2021), 145787.
[8] K. Lee, W. Jepson, Environmental impact of desalination: A systematic review of Life Cycle Assessment, Desalination 509 (2021), 115066.
[9] Y.J. Lim, K. Goh, M. Kurihara, R. Wang, Seawater desalination by reverse osmosis: Current development and future challenges in membrane fabrication ? A review, J. Membr. Sci. 629 (2021), 119292.
[10] S. Lin, H. Zhao, L. Zhu, T. He, S. Chen, C. Gao, L. Zhang, Seawater desalination technology and engineering in China: A review, Desalination 498 (2021), 114728.
[11] C. Chen, X. Geng, W. Huang, Adsorption of 4-chlorophenol and aniline by nanosized activated carbons, Chem. Eng. J. 327 (2017) 941–952.
[12] D. Huang, G. Wang, Z. Shi, Z. Li, F. Kang, F. Liu, Removal of hexavalent chromium in natural groundwater using activated carbon and cast iron combined system, J. Cleaner Prod. 165 (2017) 667–676.
[13] W. Zhang, T. Xiao, N. Liu, W. Ying, The removal of chlorinated aliphatic hydrocarbons from water using reactive activated carbon: the influence of synthesis factors and reaction environments, Environ. Technol. 39 (2018) 1328–1339.
[14] C. Kim, S.S. Lee, K.T. Kwan, J. Lee, W. Li, B.J. Lafferty, D.E. Giammar, J.D. Fortner, Surface functionalized nanoscale metal oxides for arsenic(V), chromium(VI), and uranium(VI) sorption: considering single- and multi-sorbate dynamics, Environ. Sci, NANO 7 (2020) 3805–3813.
[15] X. Jiang, H. Rui, G. Chen, B. Xing, Facile synthesis of multifunctional bone biochar composites decorated with Fe/Mn oxide micro-nanoparticles: Physicochemical properties, heavy metals sorption behavior and mechanism, J. Hazard. Mater. 399 (2020), 123067.
[16] M.H. Su, D.C.W. Tsang, X.Y. Ren, Q.P. Shi, J.F. Tang, H.G. Zhang, L.J. Kong, L. A. Hou, G. Song, D.Y. Chen, Removal of U(VI) from nuclear mining effluent by porous hydroxyapatite: Evaluation on characteristics, mechanisms and performance, Environ. Pollut 254 (2019), 112891.
[17] D. Humelnicu, C. Blegescu, D. Ganju, Removal of uranium(VI) and thorium(IV) ions from aqueous solutions by functionalized silica: kinetic and thermodynamic studies, J. Radioanal. Nucl. Chem. 299 (2014) 1183–1190.
[18] T.M. Budnyak, A.V. Strizhak, A. Gladysz-Plaska, D. Sternik, I.V. Komarov, D. Kolodynska, M. Majdan, V.A. Tertykh, Silica with immobilized phosphinic acid-derivative for uranium extraction, J. Hazard. Mater. 314 (2016) 326–340.
[19] A. Gladysz-Plaska, E. Skwarek, T.M. Budnyak, D. Kolodynska, Metal ions removal using nano oxide pyrolox (TM) material, Nanoscale Res. Lett. 12 (2017).
[20] S. Song, K. Wang, Y.H. Zhang, Y.K. Wang, C.L. Zhang, X. Wang, R. Zhang, J. R. Chen, T. Wen, X.K. Wang, Self-assembly of graphene oxide/PEDOT:PSS nanocomposite as a novel adsorbent for uranium immobilization from wastewater, Environ. Pollut 250 (2019) 196–205.
[21] L. Yin, P.Y. Wang, T. Wen, S.J. Yu, X.X. Wang, T. Hayat, A. Alsaedi, X.K. Wang, Synthesis of layered titanate nanowires at low temperature and their application in efficient removal of U(VI), Environ. Pollut 226 (2017) 125–134.
[22] D. Bontea, C. Mita, D. Humelnicu, Removal of uranyl ions from wastewaters using cellulose and modified cellulose materials, J. Radioanal. Nucl. Chem. 268 (2006) 305–311.
[23] L.J. Kong, H.M. Zhang, W. Ji, K.M. Shih, M.H. Su, Z.H. Diao, R.M. Xu, L.A. Hou, G. Song, D.Y. Chen, Recovery of phosphorus rich krill shell biowaste for uranium immobilization: A study of sorption behavior, surface reaction, and phase transformation, Environ. Pollut 243 (2018) 630–636.
[24] S.N. Guilhen, S. Rovani, L.G.d. Araujo, J.A.S. Tenório, O. Mašek, Uranium removal from aqueous solution using macauba endocarp-derived biochar: Effect of physical activation, Environ. Pollut 272 (2021), 116022.
[25] M. Nasrollahzadeh, M. Sajjadi, S. Iravani, R.S. Varma, Starch, cellulose, pectin, gum, alginate, chitin and chitosan derived (nano) materials for sustainable water treatment: A review, Carbohydr. Polym. 251 (2021), 116986.
[26] E. Guibal, Interactions of metal ions with chitosan-based sorbents: a review, Sep. Purif. Technol. 38 (2004) 43–74.
[27] X. Gao, C. Guo, J. Hao, Z. Zhao, H. Long, M. Li, Adsorption of heavy metal ions by sodium alginate based adsorbent-a review and new perspectives, Int. J. Biol. Macromol. 164 (2020) 4423–4434.
[28] Z.A. Sutirman, M.M. Sanagi, W.I.W. Aini, Alginate-based adsorbents for removal of metal ions and radionuclides from aqueous solutions: A review, Int. J. Biol. Macromol. 174 (2021) 216–228.
[29] L. Zhou, H. Zou, Y. Wang, Z. Liu, Z. Le, G. Huang, T. Luo, A.A. Adesina, Immobilization of in situ generated Fe-0-nanoparticles in tripolyphosphate-crosslinking chitosan membranes for enhancing U(VI) adsorption, J. Radioanal. Nucl. Chem. 311 (2017) 779–787.
[30] Z. Huang, Z. Li, L. Zheng, L. Zhou, Z. Chai, X. Wang, W. Shi, Interaction mechanism of uranium(VI) with three-dimensional graphene oxide-chitosan composite: Insights from batch experiments, IR, XPS, and EXAFS spectroscopy, Chem. Eng. J. 328 (2017) 1066–1074.
[31] X. Tang, L. Zhou, Z. Le, Y. Wang, Z. Liu, G. Huang, A.A. Adesina, Preparation of porous chitosan/carboxylated carbon nanotube composite aerogels for the efficient removal of uranium(VI) from aqueous solution, Int. J. Biol. Macromol. 160 (2020) 1000–1008.
[32] M.F. Hamza, Y. Wei, A. Benettayeb, X. Wang, E. Guibal, Efficient removal of uranium, cadmium and mercury from aqueous solutions using grafted hydrazide-micro-magnetite chitosan derivative, J. Mater. Sci. 55 (2020) 4193–4212.
[33] M.F. Hamza, A. Gamal, G. Hussein, M.S. Nagar, A.A.H. Abdel-Rahman, Y. Wei, E. Guibal, Uranium(VI) and zirconium(IV) sorption on magnetic chitosan derivatives – effect of different functional groups on separation properties, J. Chem. Technol. Biotechnol. 94 (2019) 3866–3882.
[34] Y. Liu, C. Chen, L. He, L. Hu, Z. Ding, S. Liao, N. Tan, Preparation of a fungal-modified material linked by the monoamidoxime terminal open-chain polyether and its uranyl adsorption, Ind. Eng. Chem. Res. 60 (2021) 4705–4713.
[35] M. Arvand, R. Shemshadi, A.A. Efondiov, N.A. Zeynalov, L. Latify, A. Pourhabib, R. Farnoosh, Comparative study for the removal of Hg(II) from aqueous solutions by adsorption on the gum arabic and modified gum arabic, Asian J. Chem. 22 (2010) 6289–6301.
[36] D. Das, R. Vimala, N. Das, Removal of Ag(I) and Zn(II) ions from single and binary solution using sulfonated form of gum arabic-powdered mushroom composite hollow semispheres: Equilibrium, kinetic, thermodynamic and ex-situ studies, Ecol. Eng. 75 (2015) 116–122.
[37] A. Jakobik-Kolon, J. Bok-Badura, K. Karon, K. Mitko, A. Milewski, Hybrid pectin-based biosorbents for zinc ions removal, Carbohydr. Polym. 169 (2017) 213–219.
[38] A.M. Elbedwehy, A.M. Abou-Elanwar, A.O. Ezzat, A.M. Atta, Super effective removal of toxic metals water pollutants using multi functionalized polyacrylonitrile and Arabic gum grafts, Polymers 11 (2019) 1938.
[39] A.A. El-Zahhar, S. Bondock, M. Abu Haija, S.M.A.S. Keshk, Gum Arabic dialdehyde thiosemicarbazone chelating resin for removal mercury (II) from aqueous solutions, Desalin. Water Treat. 151 (2019) 403–413.
[40] L.R. Varghese, D. Das, N. Das, Adsorptive removal of nickel(II) ions from aqueous environments using gum based and clay based polyaniline/chitosan nanobiocomposite beads and microspheres: Equilibrium, kinetic, thermodynamics and ex-situ studies, Korean J. Chem. Eng. 33 (2016) 2114–2126.
[41] Z. Sabouri, A. Akbari, H.A. Hosseini, M. Khatami, M. Darroudi, Green-based bio-synthesis of nickel oxide nanoparticles in Arabic gum and examination of their cytotoxicity, photocatalytic and antibacterial effects, Green Chem. Lett. Rev. 14 (2021) 402–412.
[42] N.M. Jalal, A.R. Jabur, M.S. Hamza, S. Allami, The effect of sulfonation reaction time on polystyrene electrospun membranes as polymer electrolyte, AIP Conf. Proc. 2290 (2020), 020049.
[43] S.D. Alexandratos, From ion exchange resins to polymer-supported reagents: an evolution of critical variables, J. Chem. Technol. Biotechnol. 93 (2018) 20–27.
[44] S.D. Alexandratos, X. Zhu, The effect of hydrogen bonding in enhancing the ionic affinities of immobilized monoprotic phosphate ligands, Materials 10 (2017) 10080968.
[45] S.D. Alexandratos, X. Zhu, The role of polarizability in determining metal ion affinities in polymer-supported reagents: monoprotic phosphates and the effect of hydrogen bonding, New J. Chem. 39 (2015) 5366–5373.
[46] C. Valgas, S.M. de Souza, E.F.A. Smania, A. Smania, Screening methods to determine antibacterial activity of natural products, Braz. J. Microbiol. 38 (2007) 369–380.
[47] E.F. El-Belely, M.M.S. Farag, H.A. Said, A.S. Amin, E. Azab, A.A. Gobouri, A. Fouda, Green synthesis of zinc oxide nanoparticles (ZnO-NPs) using *Arthrospira platensis* (Class: *Cyanophyceae*) and evaluation of their biomedical activities, Nanomaterials 11 (2021) 11010095.
[48] O. Falyouna, O. Eljamal, I. Maamoun, A. Tahara, Y. Sugihara, Magnetic zeolite synthesis for efficient removal of cesium in a lab-scale continuous treatment system, J. Colloid Interface Sci. 571 (2020) 66–79.
[49] T.I. Shaheen, A. Fouda, S.S. Salem, Integration of cotton fabrics with biosynthesized CuO nanoparticles for bactericidal activity in the terms of their cytotoxicity assessment, Ind. Eng. Chem. Res. 60 (2021) 1553–1563.
[50] J.M. Chambers, W.S. Cleveland, B. Kleiner, P.A. Tukey, Graphical Methods for Data Analysis, Wadsworth International Group, Belmont (CA), USA, 1983pp.
[51] M. Ruiz, A. Sastre, E. Guibal, Pd and Pt recovery using chitosan gel beads. I. influence of the drying process on diffusion properties, Sep. Sci. Technol. 37 (2002) 2143–2166.
[52] A. Djelad, A. Morsli, M. Robitzer, A. Bengueddach, F. di Renzo, F. Quignard, Sorption of Cu(II) ions on chitosan-zeolite X composites: Impact of gelling and drying conditions, Molecules 21 (2016) 0109.
[53] M.J. Zohuriaan, F. Shokrolahi, Thermal studies on natural and modified gums, Polym. Test. 23 (2004) 575–579.
[54] Y.H. Gad, Preparation and characterization of poly(2-acrylamido-2-methylpropane-sulfonic acid)/Chitosan hydrogel using gamma irradiation and its application in wastewater treatment, Radiat. Phys. Chem. 77 (2008) 1101–1107.
[55] M.A. Hubbe, S. Azizian, S. Douven, Implications of apparent pseudo-second-order adsorption kinetics onto cellulosic materials: A review, BioResources 14 (2019) 7582–7626.
[56] Y. Marcus, Ion Properties, Marcel Dekker Inc, New York, NY, 1997, p. 259.
[57] I.H. Zidan, M.F. Cheira, A.R. Bakry, B.M. Atia, Potentiality of uranium recovery from G.Gattar leach liquor using Duolite ES-467 chelating resin: Kinetic, thermodynamic and isotherm features, Int. J. Environ. Anal. Chem. (2020) 1748613.
[58] D.A. Giannakoudakis, I. Anastopoulos, M. Barczak, E. Alphantoniou, K. Terpilowski, E. Mohammadi, M. Shams, E. Coy, A. Bakandritsos, I. A. Katsoyiannis, et al., Enhanced uranium removal from acidic wastewater by phosphonate-functionalized ordered mesoporous silica: Surface chemistry matters the most, J. Hazard. Mater. 413 (2021), 125279.
[59] P. Amesh, K.A. Venkatesan, A.S. Suneesh, N. Samanta, Diethylenetriamine tethered mesoporous silica for the sequestration of uranium from aqueous solution and seawater, J. Environ. Chem. Eng. 8 (2020), 103995.

[60] D.X. He, N. Tan, X.M. Luo, X.C. Yang, K. Ji, J.W. Han, C. Chen, Y.Q. Liu, Preparation, uranium (VI) absorption and reuseability of marine fungus mycelium modified by the bis-amidoxime-based groups, Radiochim. Acta 108 (2020) 37–49.
[61] R.G. Pearson, Acids and bases, Science (New York, N.Y.), 151 (1966) 172-177.
[62] A.S. Hicyilmaz, A.K. Seckin, I. Cerkez, Synthesis, characterization and chlorination of 2-acrylamido-2methylpropane sulfonic acid sodium salt-based antibacterial hydrogels, React. Funct. Polym. 115 (2017) 109–116.
[63] A.S. Elfeky, S.S. Salem, A.S. Elzaref, M.E. Owda, H.A. Eladawy, A.M. Saeed, M. A. Awad, R.E. Abou-Zeid, A. Fouda, Multifunctional cellulose nanocrystal/metal oxide hybrid, photo-degradation, antibacterial and larvicidal activities, Carbohydr. Polym. 230 (2020), 115711.
[64] M.F. Hamza, N.A. Hamad, D.M. Hamad, M.S. Khalafalla, A.A.H. Abdel-Rahman, I. F. Zeid, Y. Wei, M.M. Hessien, A. Fouda, W.M. Salem, Synthesis of eco-friendly biopolymer, alginate-chitosan composite to adsorb the heavy metals, Cd(II) and Pb (II) from contaminated effluents, Materials 14 (2021) 2189.
[65] G. Martinez de Tejada, S. Sanchez-Gomez, I. Razquin-Olazaran, I. Kowalski, Y. Kaconis, L. Heinbockel, J. Andrae, T. Schuerholz, M. Hornef, A. Dupont, et al., Bacterial cell wall compounds as promising targets of antimicrobial agents I. Antimicrobial peptides and lipopolyamines, Curr. Drug Targets 13 (2012) 1121–1130.
[66] S.S. Salem, A. Fouda, Green synthesis of metallic nanoparticles and their prospective biotechnological applications: an overview, Biol. Trace Elem. Res. 199 (2021) 344–370.
[67] Z. Kanwal, M.A. Raza, S. Riaz, S. Manzoor, A. Tayyeb, I. Sajid, S. Naseem, Synthesis and characterization of silver nanoparticle-decorated cobalt nanocomposites (Co@ AgNPs) and their density-dependent antibacterial activity, R. Soc. Open Sci. 6 (2019), 182135.
[68] A. Fouda, S.-E.-D. Hassan, E. Saied, M.F. Hamza, Photocatalytic degradation of real textile and tannery effluent using biosynthesized magnesium oxide nanoparticles (MgO-NPs), heavy metal adsorption, phytotoxicity, and antimicrobial activity, J. Environ. Chem. Eng. 9 (2021), 105346.
[69] S.-M. Taghizadeh, N. Lal, A. Ebrahiminezhad, F. Moeini, M. Seifan, Y. Ghasemi, A. Berenjian, Green and economic fabrication of zinc oxide (ZnO) nanorods as a broadband UV blocker and antimicrobial agent, Nanomaterials 10 (2020) 530.
[70] A. Fouda, M.A. Awad, A.M. Eid, E. Saied, M.G. Barghoth, M.F. Hamza, M.F. Awad, S. Abdelbary, S.-E.-D. Hassan, An eco-friendly approach to the control of pathogenic microbes and *Anopheles stephensi* malarial vector using magnesium oxide nanoparticles (Mg-NPs) fabricated by *Penicillium chrysogenum*, Int. J. Mol. Sci. 22 (2021) 5096.
[71] B. Veeraswamy, D. Madhu, G.J. Dev, Y. Poornachandra, G.S. Kumar, C.G. Kumar, B. Narsaiah, Studies on synthesis of novel pyrido 2,3-d pyrimidine derivatives, evaluation of their antimicrobial activity and molecular docking, Bioorg. Med. Chem. Lett. 28 (2018) 1670–1675.
[72] L. Yin, X. Zhao, L. Cui, J. Ding, M. He, C. Tang, C. Yin, Cytotoxicity and genotoxicity of superporous hydrogel containing interpenetrating polymer networks, Food Chem. Toxicol. 47 (2009) 1139–1145.
[73] S. Bang, U.-W. Jung, I. Noh, Synthesis and biocompatibility characterizations of in situ chondroitin sulfate–gelatin hydrogel for tissue engineering, J. Tissue Eng. Regener. Med. 15 (2018) 25–35.
[74] N.T.H. Nga, T.T.B. Ngoc, N.T.M. Trinh, T.L. Thuoc, D.T.P. Thao, Optimization and application of MTT assay in determining density of suspension cells, Anal. Biochem. 610 (2020), 113937.
[75] A. Shukla, A.P. Singh, P. Maiti, Injectable hydrogels of newly designed brush biopolymers as sustained drug-delivery vehicle for melanoma treatment, Signal Transduction Targeted Ther. 6 (2021) 63.
[76] I. Lashin, A. Fouda, A.A. Gobouri, E. Azab, Z.M. Mohammedsaleh, R.R. Makharita, Antimicrobial and in vitro cytotoxic efficacy of biogenic silver nanoparticles (Ag-NPs) fabricated by callus extract of *Solanum incanum* L, Biomolecules 11 (2021) 341.
[77] E.S. Al-Sheddi, N.N. Farshori, M.M. Al-Oqail, S.M. Al-Massarani, Q. Saquib, R. Wahab, J. Musarrat, A.A. Al-Khedhairy, M.A. Siddiqui, Anticancer potential of green synthesized silver nanoparticles using extract of *Nepeta deflersiana* against human cervical cancer cells (HeLA), Bioinorg. Chem. Appl. 2018 (2018) 9390784.
[78] A.M. Eid, A. Fouda, G. Niedbala, S.-E.-D. Hassan, S.S. Salem, A.M. Abdo, H. F. Hetta, T.I. Shaheen, Endophytic *Streptomyces laurentii* mediated green synthesis of Ag-NPs with antibacterial and anticancer properties for developing functional textile fabric properties, Antibiotics-Basel 9 (2020) 641.
[79] C.A. Dos Santos, M.M. Seckler, A.P. Ingle, I. Gupta, S. Galdiero, M. Galdiero, A. Gade, M. Rai, Silver nanoparticles: Therapeutical uses, toxicity, and safety issues, J. Pharm. Sci. 103 (2014) 1931–1944.